Supporting Information

Designing Ternary Hydrated Eutectic Electrolyte Capable of Four-Electron Conversion for Advanced Zn-I_2 Full Batteries

Wenda Li[a], Hengyue Xu[b], Hongyi Zhang[a], Facai Wei[a], Tingting Zhang[a], Yong Wu[a], Lingyan Huang[a], Jianwei Fu[c], Chengbin Jing[a], Jiangong Cheng[d], Shaohua Liu*[a]

[a] State Key Laboratory of Precision Spectroscopy; Engineering Research Center of Nanophotonics & Advanced Instrument, Ministry of Education, School of Physics and Electronic Science, East China Normal University, Shanghai, 200241, P.R. China, E-mail: shliu@phy.ecnu.edu.cn

[b] Institute of Biopharmaceutical and Health Engineering, Tsinghua Shenzhen International Graduate School, Tsinghua University, Shenzhen 518055, China

[c] School of Materials Science and Engineering, Zhengzhou University,75 Daxue Road, Zhengzhou, 450052, P. R. China

[d] State Key Lab of Transducer Technology Shanghai Institute of Microsystem and Information Technology, Chinese Academy of Sciences, Shanghai 200050, P. R. China,

1. Experimental Procedures

1.1 Chemicals and Materials

Niacinamide (NA) and Dimethyl sulfone (DMS) (99% purity) were purchased from Aladdin. Both $Zn(ClO_4)_2{\cdot}6H_2O$ and zinc trifluoromethylsulfonimide abbreviated as $Zn(OTf)_2$ were purchased from Macklin. PVDF binder with an average MW of ~1,000,000 is provided by Sigma-Aldrich. N-methyl-2-pyrrolidone (NMP, 99.9% purity) was purchased from Aladdin. Conductive carbon black (AR, 99% purity) was purchased from Aladdin. Glass fiber separator (Whatman GF/A) with a thickness of 260 μm was purchased from Sigma-Aldrich. Carbon cloth with a thickness of 0.02 mm is purchased from Shanghai Hesen electric Co., LTD. Zinc foil with a thickness of 0.03 mm is purchased from Wenzhou metal materials commercial company. Iodine powder was purchased from Beijing Ionochem technology Co., LTD. KI and ICl powder was purchased from Adamas Co., LTD.

1.2 Electrolyte/Electrode preparation and coin cell assembly

The zinc-based ternary hydrated eutectic electrolytes (ZTEs) were prepared by mixing niacinamide (NA), dimethyl sulfone (DMS), and $Zn(ClO_4)_2{\cdot}6H_2O$ after heating at 80 °C and then cooling at room temperature (the optimal molar ratio of NA, DMS to $Zn(ClO_4)_2{\cdot}6H_2O$ is 0.5:3:1). In addition, the 1M $Zn(ClO_4)_2$ electrolyte (ZW) was prepared at room temperature was prepared as a reference. The I_2-composed cathode was prepared in the gas-adsorption method. In brief, conductive carbon black and iodine (weight ratio: 1:3) were homogeneously mixed and then heated at 120 ^oC for 12 h in vacuum-sealed. Then the I_2@C was collected after heating to 60 ^oC for 5 h to remove excess iodine. The iodine cathode (80 wt.%) (iodine content 25 wt.%) was here prepared by mixing 80 wt.% of I_2@C, 10 wt.% of Super P as a conductive agent, and 10 wt.% of PVDF as the binder in NMP solvent and cast onto a clean carbon cloth that was cut into small disks with a diameter of 12 mm. The loading for the I_2@C composite is 1.5 mg cm^{-2} for electrochemistry tests. Coin cells were assembled with glass fibber as a separator, I_2@C served as cathode and Zn as anode, each cell contains 100 μL of ZTEs or ZW electrolyte. In the fabrication of Zn//I_2 pouch cell, the prepared I_2@C composite was directly applied as the active cathode materials. The active cathode materials were mixed with conductive carbon black and PVDF in an agate mortar at a ratio of 8:1:1, using N-methyl-2-pyrrolidone (NMP) as the solvent. The above slurry was then scratched onto a piece of carbon cloth (5cm×8cm). The mass loading of the active material was 0.8 mg cm^{-2}. The typical weight

of Zn foil is 13 mg cm^{-2}, and its thickness was ~20 μm. The electrolyte was using ZTEs electrolyte. Then, the cathode, glass fiber (applied as the separator, Whatman, GF/A) and anode Zn foil were assembled into a pouch cell for further investigation.

1.3 Electrochemical measurements.

The electrochemical performances of symmetrical Zn//Zn cells, Zn//Ti cells, and Zn-I_2 batteries were studied in 2032-type coin cells at room temperature. Galvanostatic cycling tests were conducted on a multichannel battery tester in the voltage range of 0.5-1.9 V (vs. Zn/Zn^{2+}). The specific capacities of the Zn-I_2 batteries were calculated based on the mass of iodine. Impedance measurements were performed using (CHI-760E) within a frequency range of 1 MHz to 0.1 Hz. The CV measurements were performed from 0.5 to 1.9 V on CHI-760E electrochemical workstation at scan rates varying from 1.0 to 3.0 mV s^{-1}.

2. Characterization.

The morphologies of Zn deposits on the Zn-metal anodes were detected by SEM (GeminiSEM-450, Zeiss). The Raman spectra were collected on an inVia Reflex system with an excitation wavelength of 532 nm. XPS spectra were carried out using a Thermo Kalpha equipped with Al Kα X-ray source. UV–vis spectrum characterization was carried out on a Lambda950 with a range from 200 to 1200 nm. FTIR measurements were performed on a Perkin-Elmer spectrometer in the reflection mode. XRD measurements were conducted in a Rying-AXS diffractometer (D8 ADVANCE) employing Cu Kα radiation (λ = 1.5405 Å).

3. Calculation methods.

The ab initio molecular dynamics (AIMD) simulations for revealing the Zn^{2+} coordinate structures of the electrolyte were performed using Vienna Ab initio simulation package (VASP). The exchange correlation function is processed by means of the Perdew-Burke-Ernzerhof (PBE) formulate Generalized Gradient Approximation (GGA). The projector-augmented wave method was applied to describe the interaction between the atomic core and electrons. The plane-wave basis cutoff energy was set to 400 eV. All structures were fully relaxed without restriction to optimize, and the electronic step's convergence criteria were set to < 1×10^{-6} eV. The time step is set as 1.0 fs, and 1 × 1 × 1 k-point Gamma (Γ) centered Monkhorst-Pack mesh sampling is used. The Nose–Hoover thermostat was utilized to maintain the canonical temperature at 300 K. After 5 ps of pre-balancing, 30 ps of AIMD was used for data analysis. The Electrostatic potential (ESP) is plotted using Multiwfn. The

adsorption energy (E_a) in NA/DMS-Zn^{2+}/I^+ system was used to describe the interaction between Zn matrix (or I^+) and organic ligands. The energy of isolated ligand and Zn matrix (or I^+) is defined as E_l and E_{Zn} (or E_l^+), and E_{total} represents whole system energy.

$$E_a = E_{total} - E_l - E_{Zn} \text{ (or } E_l^+)$$

4. Supplementary Figures

Figure S1. (a) Scheme for preparing the ZTEs. (b) Optical photographs of preparated ZTEs in a predetermined $Zn(ClO_4)_2{\cdot}6H_2O$/DMS/NA with molar ratio of 1:3:0.5.

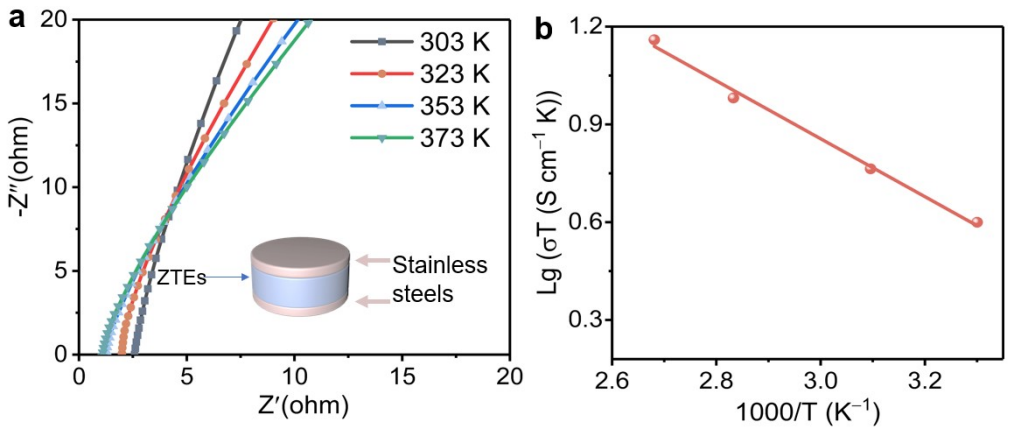

Figure S2. (a) EIS measurements made over a range of temperatures from 303 to 373 K. (b) Arrhenius plot of ionic conductivity as a function of temperature.

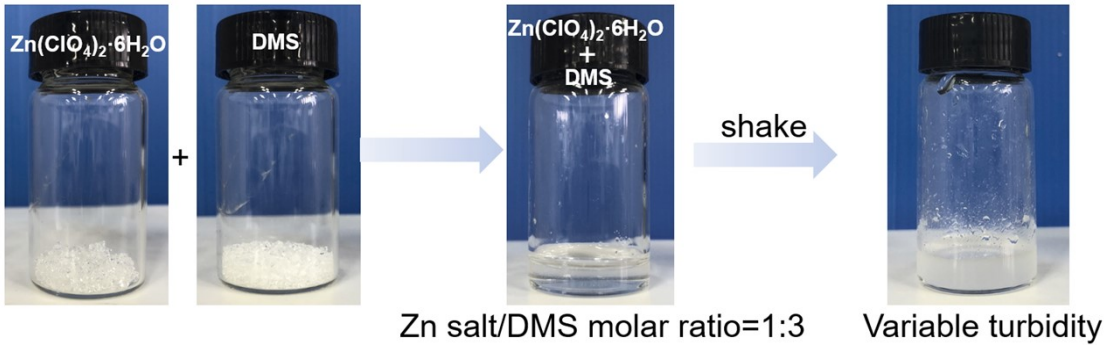

Figure S3. Scheme for preparing the ZTE in a predetermined $Zn(ClO_4)_2 \cdot 6H_2O$/DMS molar ratio of 1:3.

Note: The formed ZTEs in a predetermined $Zn(ClO_4)_2 \cdot 6H_2O$/DMS molar ratio of 1:3 is unstable.

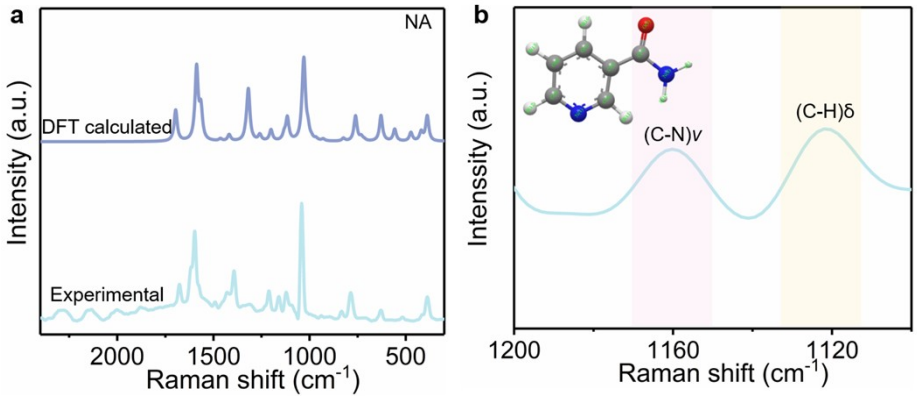

Figure S4. (a) Experimental and DFT calculated Raman spectra of NA. (b) The enlarged Raman spectrum of NA.

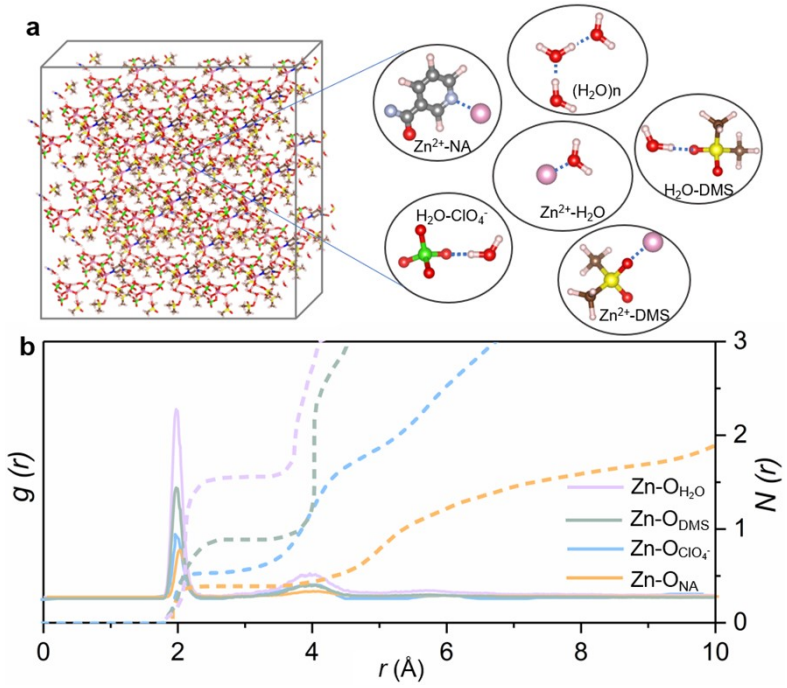

Figure S5. (a) A snapshot of ZTEs electrolyte in AIMD simulation. (b) The RDF and coordination number among Zn^{2+}, H_2O, NA, ClO_4^- and DMS.

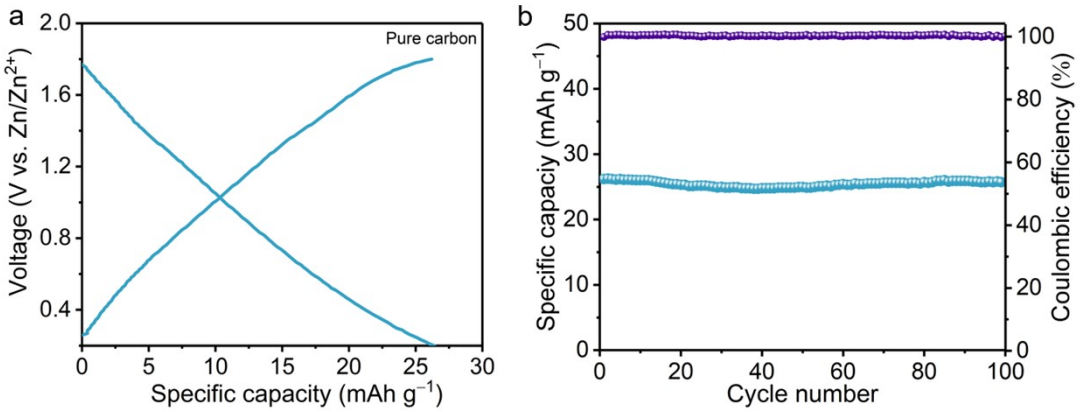

Figure S6. (a) The discharge/charge curves of pure carbon in the voltage range from 0.2-1.8 V and (b) corresponding cycling performance. (Current density: 1.0 A g^{-1}; electrolyte: ZTEs)

Note: To exclude the effect of conductive electric carbon black on the capacity for Zn-I_2 batteries, we conduct the discharge/charge measurement with carbon black served as active material under the same conditions, the battery with pure carbon as a cathode has very low capacities of 26 mAh g^{-1}. Therefore, the capacity contributed by carbon material can be neglected.

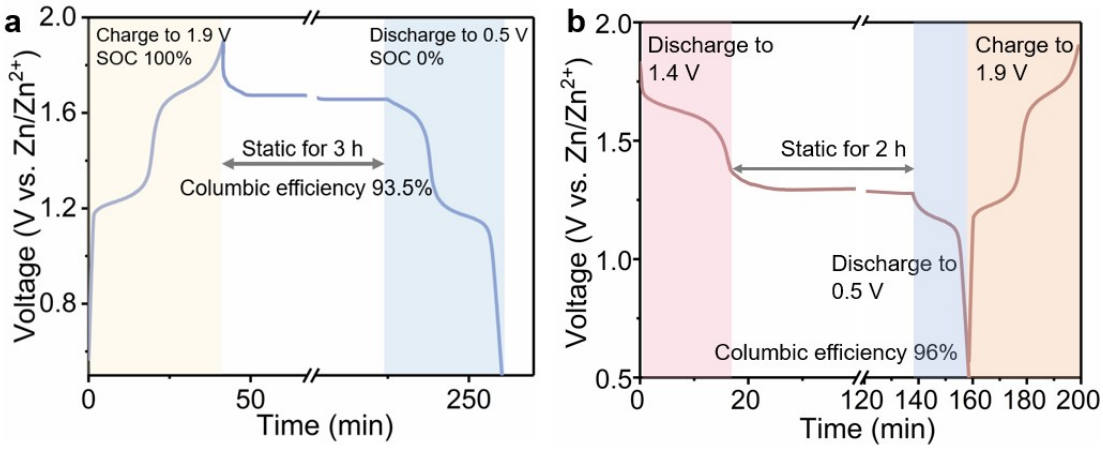

Figure S7. (a) The Zn-I_2 battery in ZTEs was first fully charged to 1.9 V at 1.0 A g^{-1} (based on active materials of cathode), and then the cells were rested at 100 % stage of charge for 3.0 h, followed by full discharging. (b) The Zn-I_2 battery in ZTEs was first discharged to 1.4 V (50 % stage of discharge) at 1.0 A g^{-1} rested for 2.0 h, and then the battery discharged to 0.5 V, followed by full discharging.

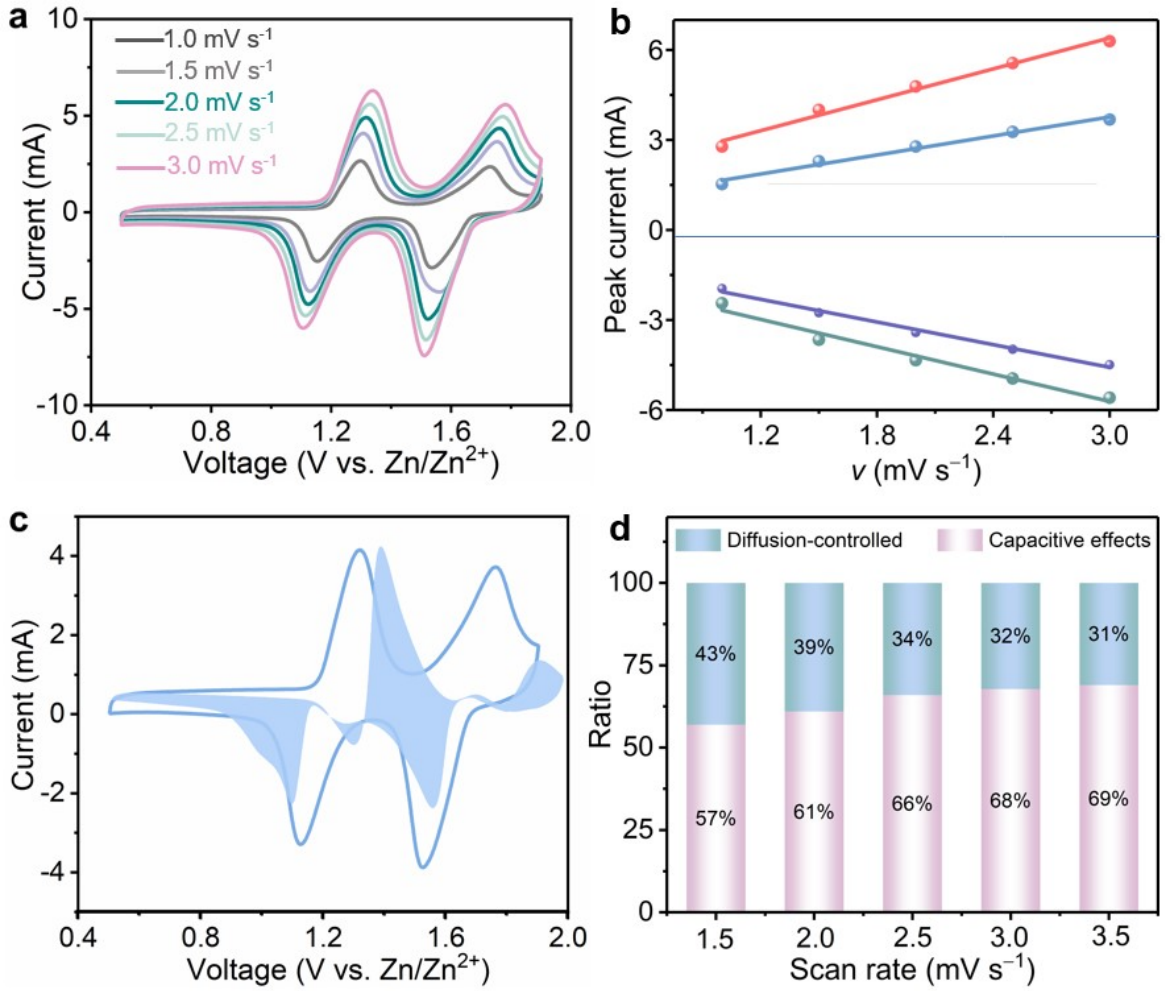

Figure S8. (a) The CV curves were obtained at different scan rates. (b) plots of *i* vs. *v* at sharp cathodic/anodic peak pair (peak current: *i*, scanning rate: *v*). (c) Capacitive contribution at 1.5 mV s^{-1}. (d) Ratios of capacitive and diffusion-controlled contribution at various scan rates.

To further understand the kinetics origin, the CV curves of the I_2@C composite cathode at various scan rates from 1.0 to 3.0 mV s^{-1} between 0.2 and 1.8 V (vs. Zn^{2+}/Zn). As shown in (a), the CV curves exhibit similar peak shape and shift during both anodic and cathodic processes. As clearly displayed, a slightly positive shift in the anodic peaks and a negative shift in the cathodic peaks can be observed with an increasing scan rate, which is caused by the polarization effect during the cycling process. The degree of the capacitive effect can be qualitatively analyzed based on the relationship between the measured current (i) and scan rate (v) from the CV curves:(1)

$$i = av^b$$

where a and b are two adjustable constants. The value of b is in the range of 0.5 to 1.0, which is determined by the slope of the log(i) vs. log(v) plot. When b is close to 1.0, the electrochemical behavior is dominated by a surface capacitive process, whereas b approaches 0.5, indicating a diffusion-controlled process. In the current experiments, the values of b for the cathodic and anodic sweep processes are calculated to be 0.73, 0.81, 0.74 and 0.89, respectively, suggesting the more significant capacitive storage kinetics of the I_2@C composite cathode in the ZTEs electrolyte.

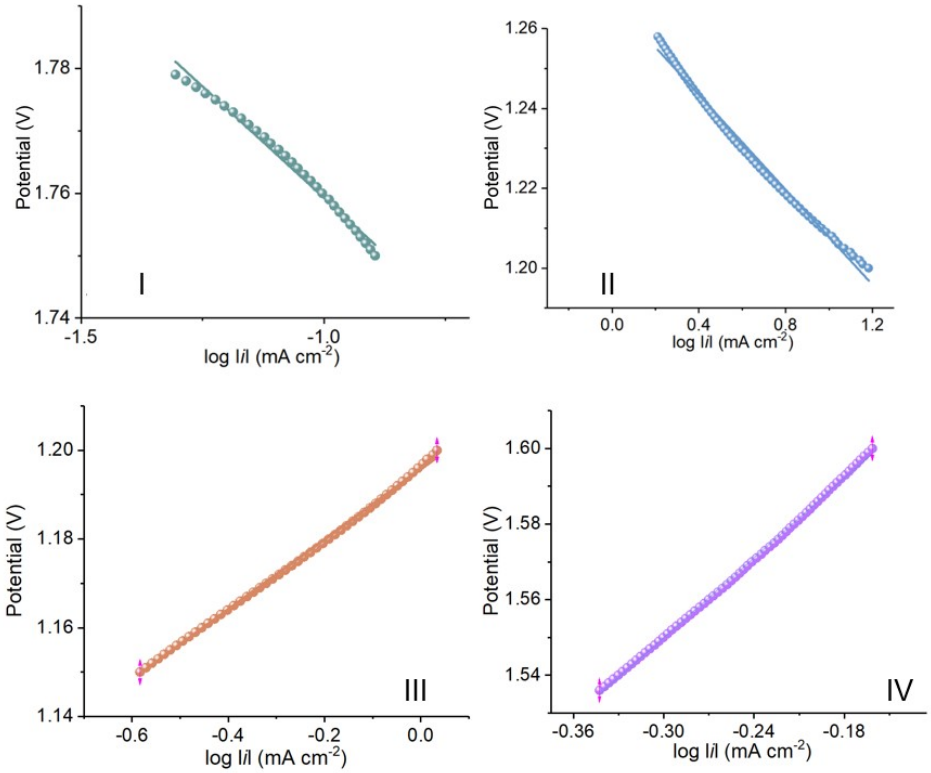

Figure S9. Reaction kinetic analysis. The Tafel slope determined from CV curves of Zn-I_2 battery with ZTEs.

Note: The Tafel slope can give information on the reaction kinetics of Zn-I_2 batteries at different redox processes based on the $I^-/I_2/I^+$ conversion enabled by ZTEs. A smaller Tafel slope is a sign of faster reaction kinetics.

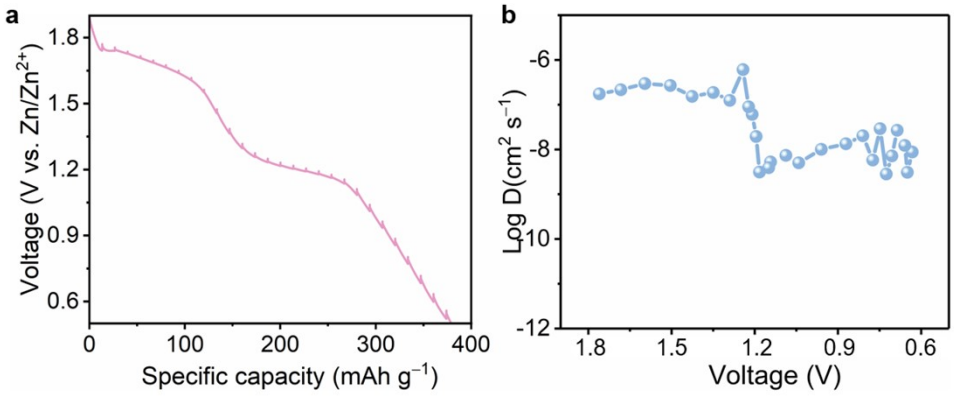

Figure S10. (a) The GITT curve of Zn-I_2 battery using ZTEs electrolyte. (b) Diffusion coefficient versus voltage calculated from GITT measurements.

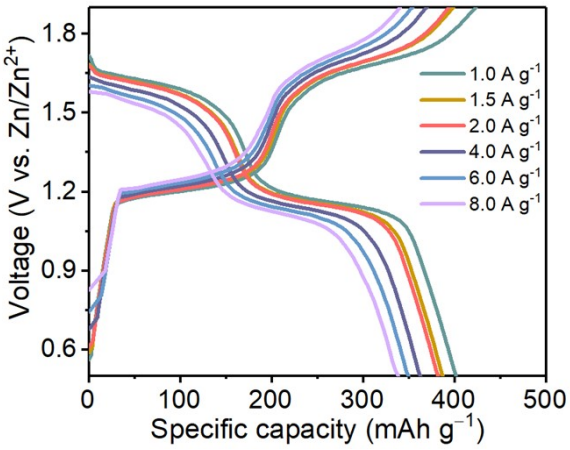

Figure S11. Voltage-capacity profiles of Zn-I_2 battery with ZTEs at various current densities.

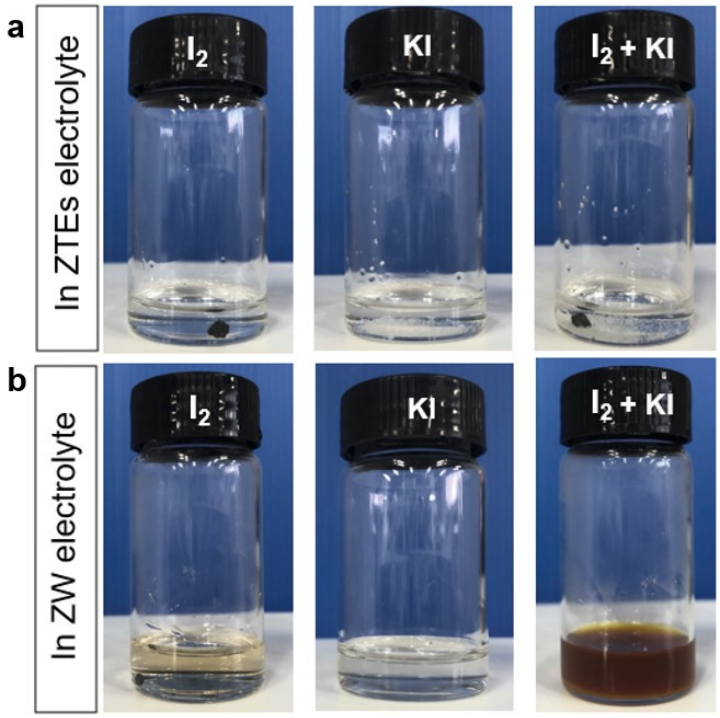

Figure S12. The solubility compared of iodine species in different electrolytes. Optical images of the KI, I_2 and KI+I_2 in (a) ZTEs and (b) ZW electrolytes, respectively.

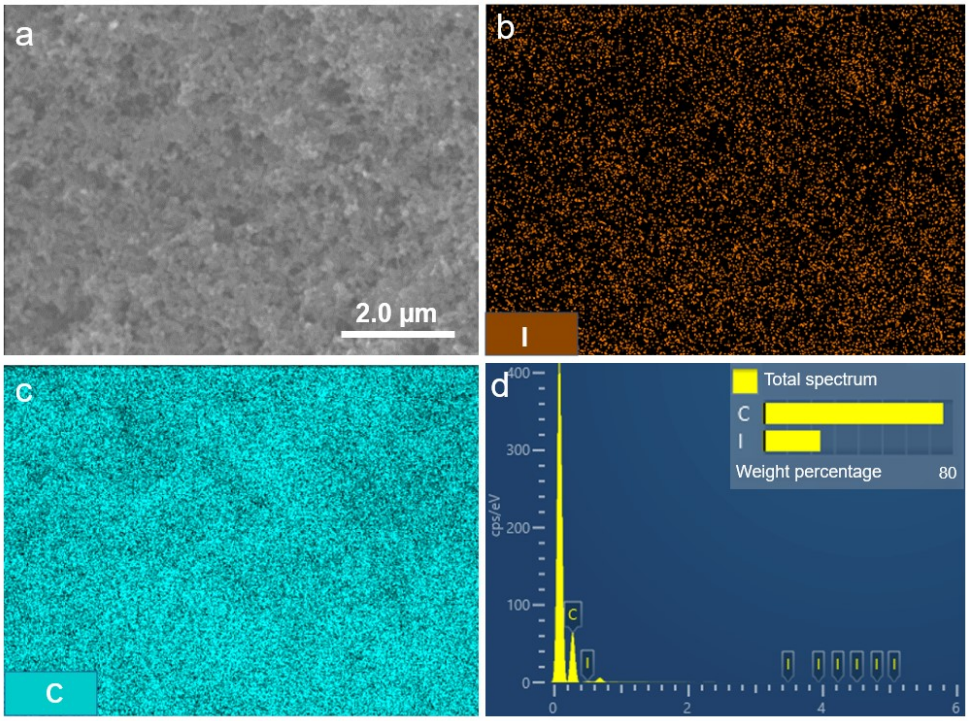

Figure S13. Elemental analysis. (a) SEM image and (b, c) element distribution maps of I_2@C composite cathode. (d) The total spectrum of element distribution.

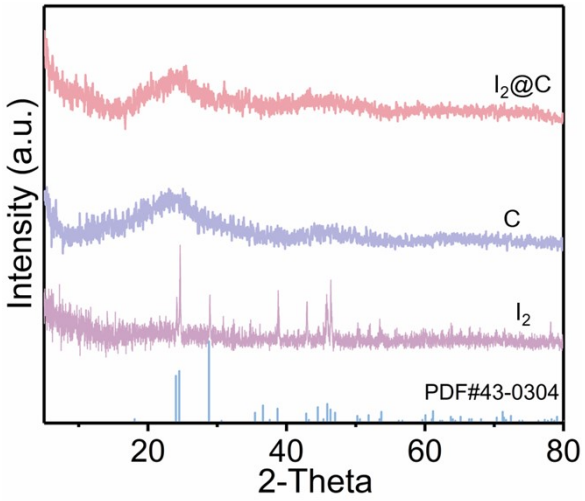

Figure S14. XRD patterns of the I_2, carbon black (C) and I_2@C composite.

Note: According to the complementary XRD measurement of the I_2@C composite cathode (Figure S14), the typical iodine diffraction peak was not detected, confirming the I_2 was adequately dispersed in carbon in the form of molecules.

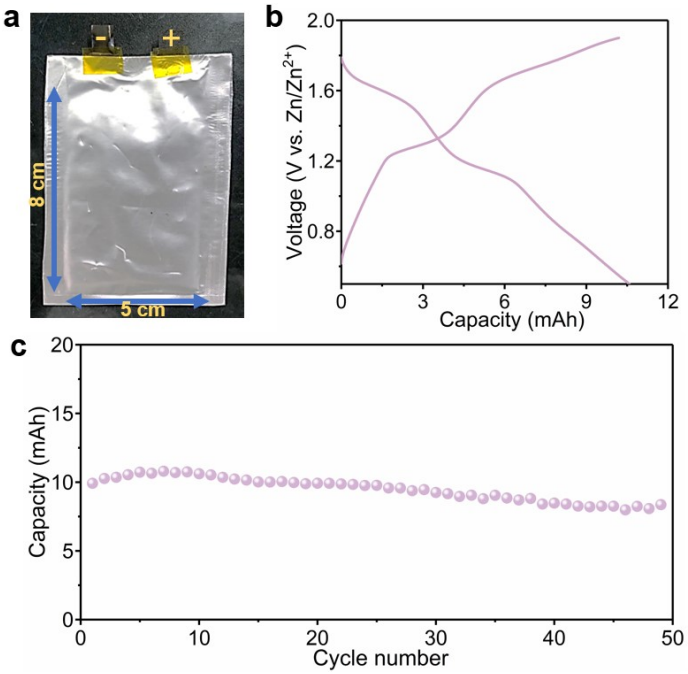

Figure S15. (a) The optical photograph of the Zn-I_2 pouch cell using ZTEs electrolyte. The charge-discharge curve (b) and cycle performance (c) of the Zn-I_2 pouch cell.

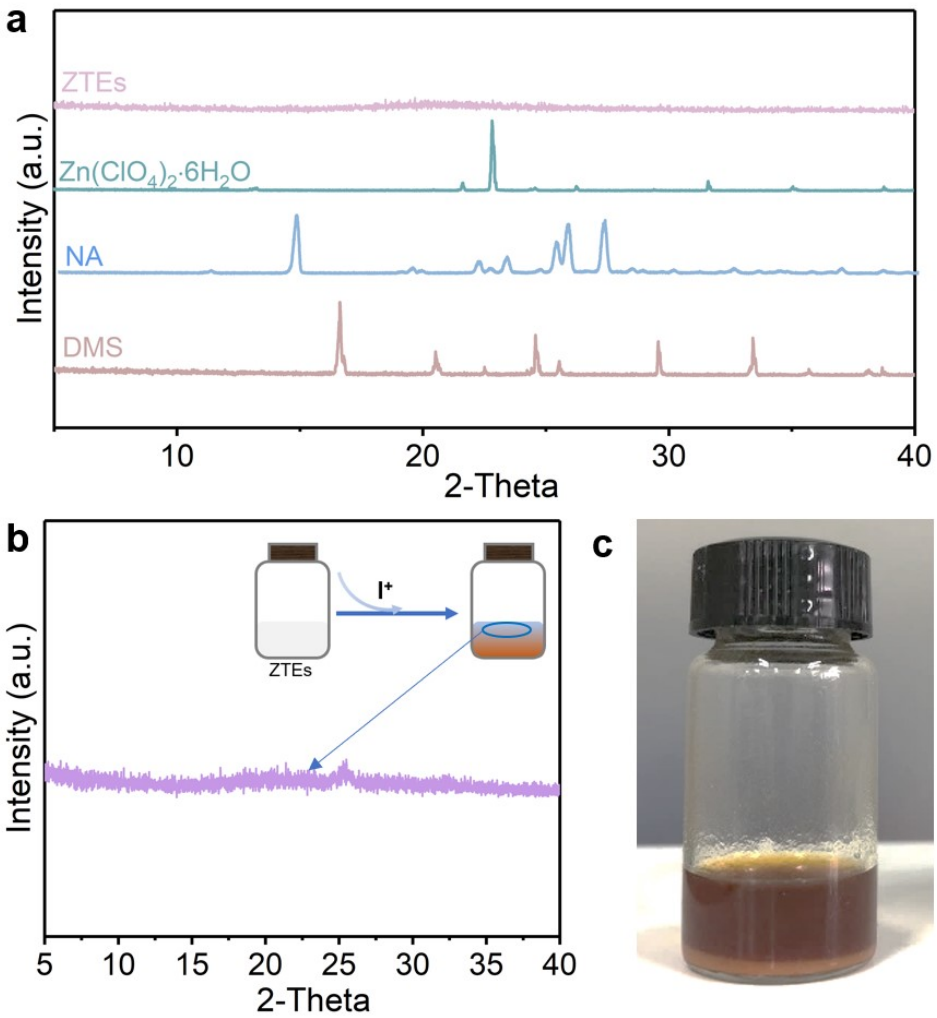

Figure S16. Crystal phase characterization. (a) The XRD parten of DMS, NA, ZN and ZTEs. (b) The XRD spectra of the supernatant were obtained after I^+ was introduced into the ZTEs electrolyte. (c) Optical images of the ZTEs electrolyte after I^+ was introduced.

Note: Obviously, the ZTEs electrolyte demonstrate a homogeneous characteristic, while the I^+ can bonded with a component of electrolyte to form precipitate. Currently, the trait makes the I^0 *in-situ* translated into stable I^+ charge-complex on the carbon matrix during charge process.

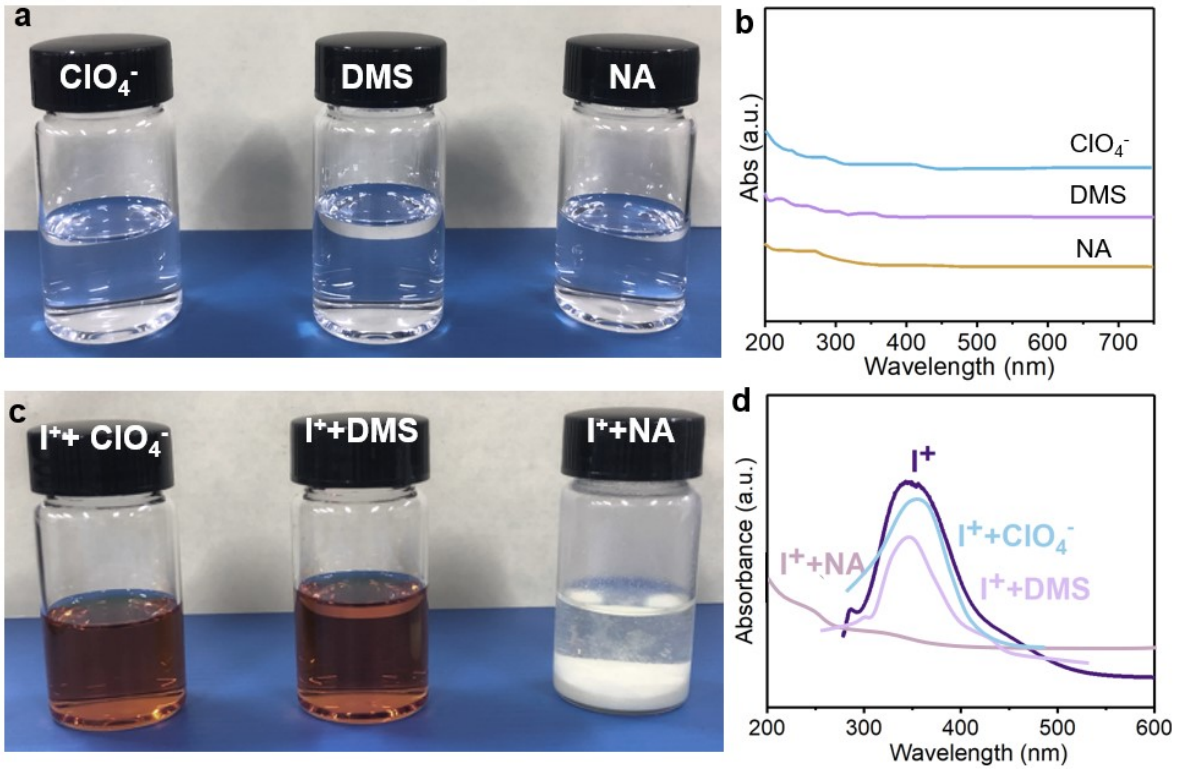

Figure S17. Characterization of force between I^+ and each component of ZTEs electrolyte. (a) Optical images of the solutions containing different ions or molecules and (b) corresponding UV-vis spectroscopy. (c) Optical images of the solutions containing different ions or molecules after adding I^+ (the molar ratio of ion or molecule to I^+=1:1).

Note: Considering that I^+ will be hydrolyzed in an aqueous solution, here we adopt anhydrous ethanol as solvent. According to the UV-vis spectral spectrum and optical images, we can conclude there exists strong action between NA and I^+ due to the rapid generation of precipitates, while the action between I^+ and ClO_4^- (and DMS) almost can be negligible.

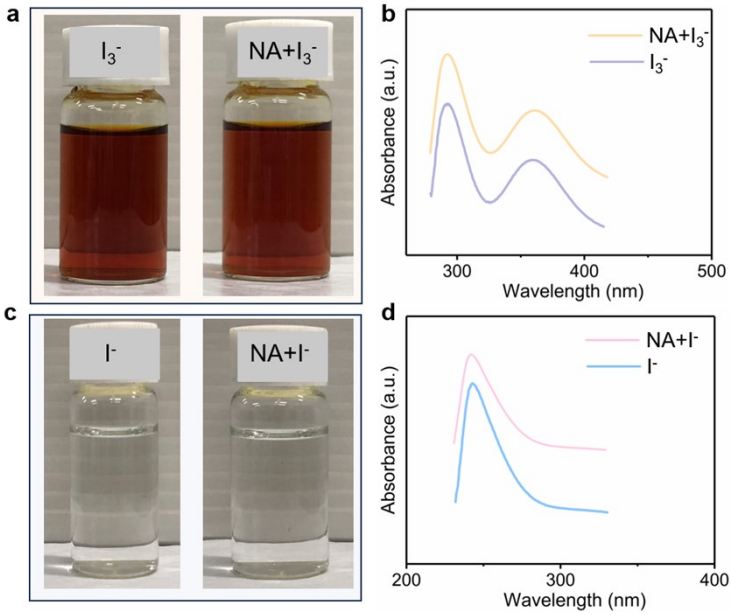

Figure S18. (a) The optical photos of I_3^- and $NA+I_3^-$ solutions (b) corresponding UV-vis spectrum. (c) The optical photos of I^- and $NA+I^-$ solutions (d) corresponding UV-vis spectrum.

Note: There is no color change and absorption peaks shift for I_3^-/$NA+I_3^-$ and I^- and $NA+I^-$ solutions, confirming that the NA molecule does have not strong interactions with iodine ions (I_3^- and I^-).

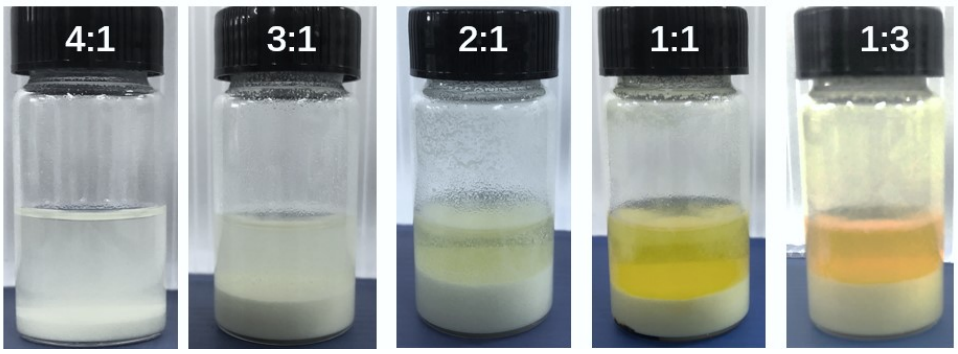

Figure S19. Study on the coordination ratio of I^+ to NA. The optical images of mixing I^+ and NA solution at different molar ratios.

Note: According to the optical images, the I^+ can be bonded steadily by NA to form a solid precipitate due to strong dipole-ions acting force. When the molar ratio of NA to I^+ more than 3, the I^+ can be sufficiently bonded. there will exist free I^+ when the ratio is less than 1. Therefore, the formed solid precipitate can be conjectured as $[I(NA)_2]^+$. The following DFT calculation also verified the conclusion.

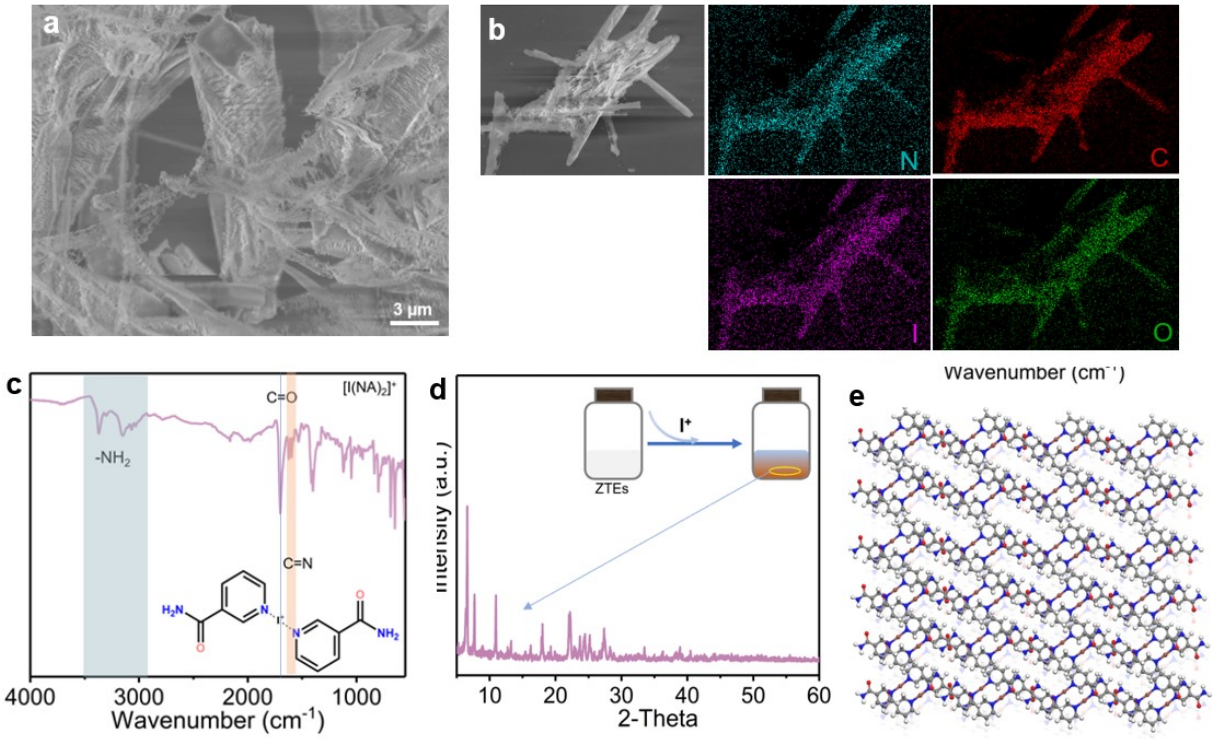

Figure S20. Structural characterization of $[I(NA)_2]^+$. (a) SEM image and (b) corresponding EDS mapping. (c) FTIR spectroscopy of $[I(NA)_2]^+$ composite. (d) XRD pattern and (e) correspnding crystal configuration.

Note: The $[I(NA)_2]^+$ can be aseembly to form specific crystal structure due to the hydrogen bonding and π-π stacking.

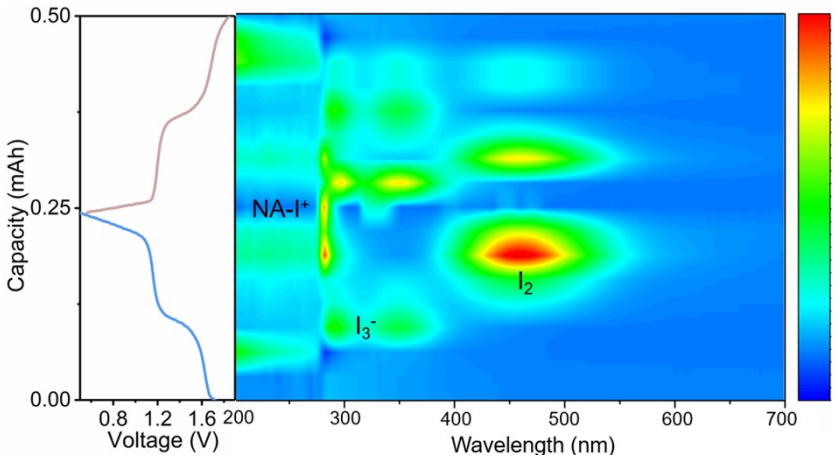

Figure S21. The *in-situ* UV-vis spectrum of the Zn-I_2 battery employing ZTEs electrolyte during discharge/charge process.

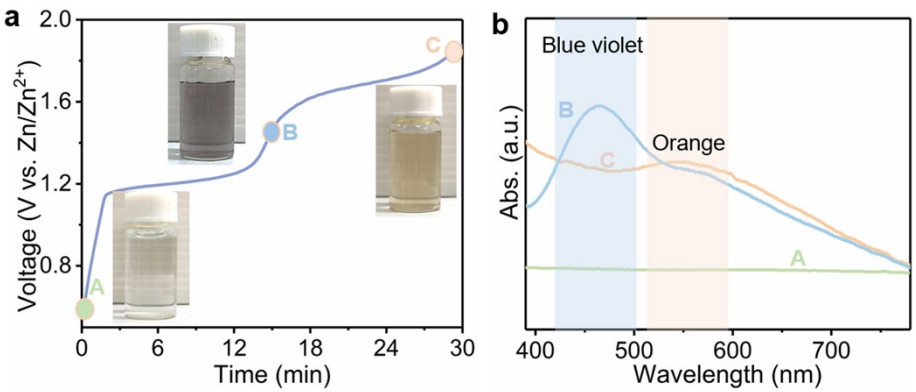

Figure S22. (a) The optical photos of the starch solution after soaking the electrodes in different states and (b) the corresponding visible absorption spectrum.

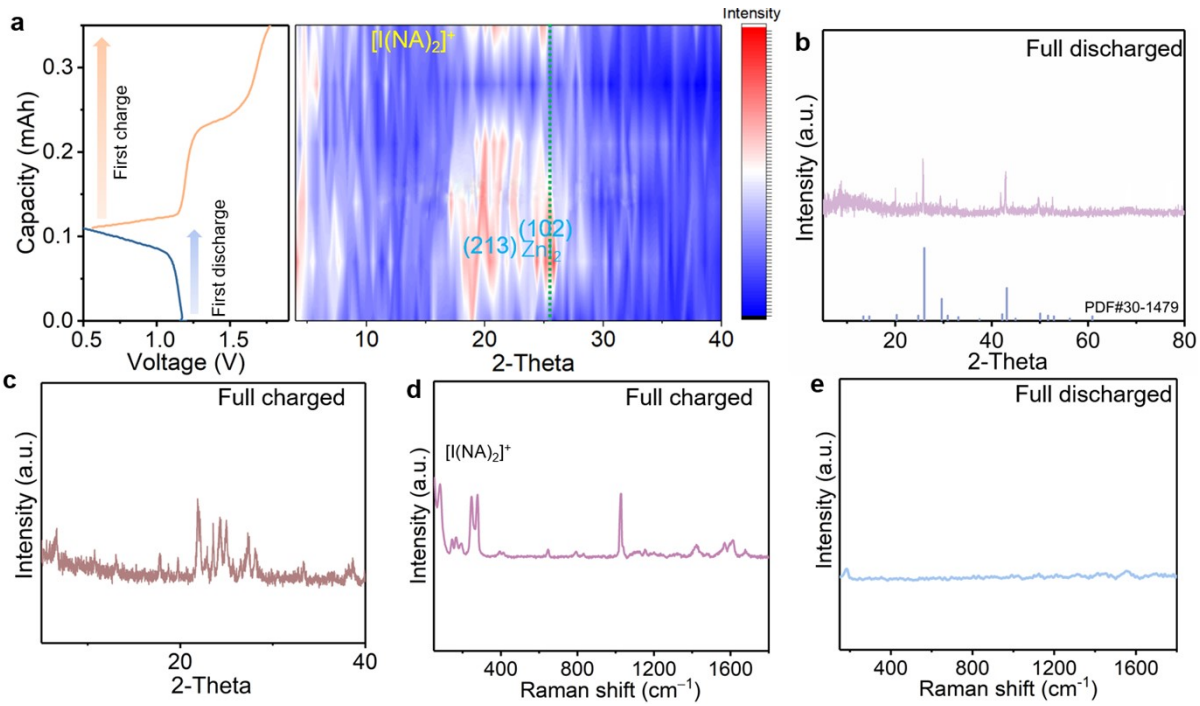

Figure S23. Evolution of iodine species. (a) The *ex-situ* XRD spectra of I_2@C cathode during charge/discharge process. (b) Corresponding XRD spectra after full discharged. (c) The corresponding XRD spectra after full charged. The Raman spectra of I_2@C cathode (d) after full charged and (e) after full discharged in ZTEs electrolyte, respectively.

Note: After full charged, the XRD spectra together with Raman spectra further confirmed that the $[I(NA)_2]^+$ is the final charging species.

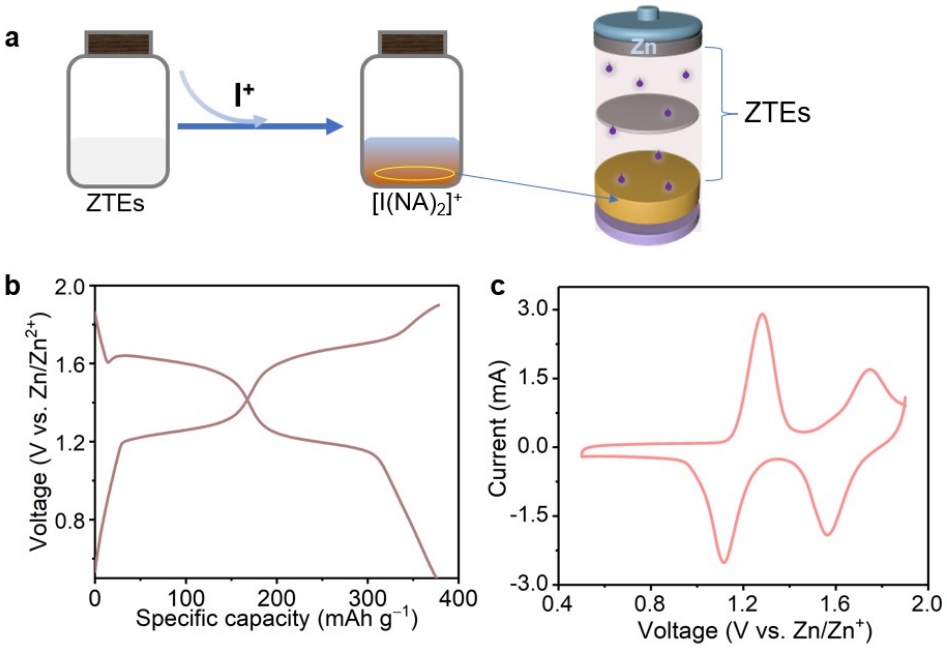

Figure S24. Performance of Zn^{2+} battery with $[I(NA)_2]^+$ as cathode. (a) Schematic diagram of assembling a Zn^{2+} battery with $[I(NA)_2]^+$ served as cathode. (b) Voltage specific capacity curve and (c) CV curve of Zn-$[I(NA)_2]^+$ battery.

Note: In order to amply confirm the hypothesis of the $[I(NA)_2]^+$ the final charging species, we performed the measurement of Zn^{2+} battery with $[I(NA)_2]^+$ as cathode. The battery shows two pairs of reversible redox peaks that corresponding $2I^-/I_2/2I^+$ four-electron conversion. Therefore, the $[I(NA)_2]^+$ can be the final charging species in our study Zn-I_2 battery system using ZTEs electrolyte.

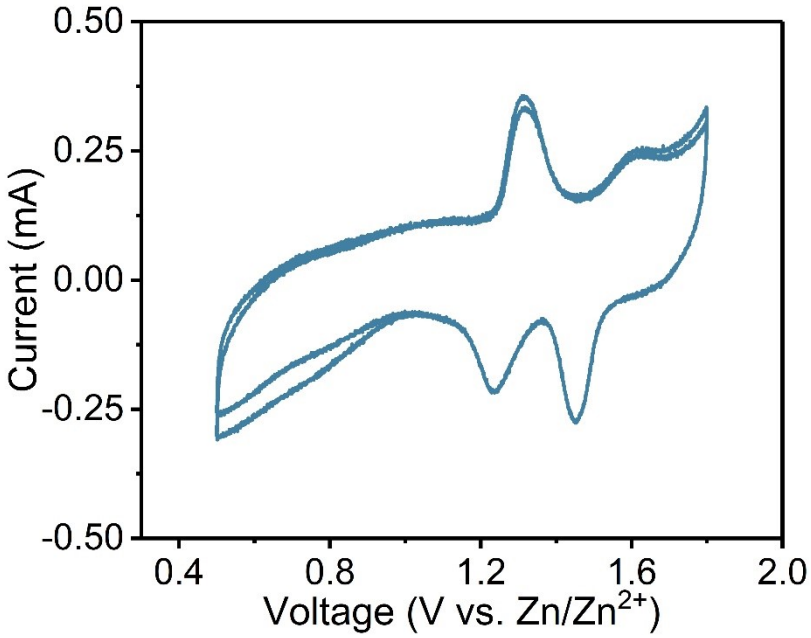

Figure S25. CV curves of Zn-I_2 battery using as I_2@C cathode and 2M $Zn(OTf)_2$+NA as electrolyte. Here, the 0.2 g NA was added to a 5mL 2M $Zn(OTf)_2$ solution ($Zn(OTf)_2$/NA) to serve as a contrast electrolyte.

Note: The previously reported literature has confirmed that the Cl^- can activate the high valance oxidation of I species. Therefore, in order to exclude ClO_4^- influence in this work, we further conducted an electrochemistry test using $Zn(OTf)_2$/NA electrolyte. Generally, there is a lot of free water in the 2M $Zn(OTf)_2$ electrolyte, which will cause hydrolysis of iodide cations. The water molecule is hydrogen bonds locked by NA to further reduce its activity by adding a large number of NA molecules, For the cell using the $Zn(OTf)_2$/NA electrolyte, the CV curves demonstrate two couples of redox peaks, suggesting the I^+ was stabilized by NA and realized the $2I^-/I_2/2I^+$ four-electron conversion in other electrolyte systems. The low potential corresponding to the redox peaks may be due to polarization. Therefore, the above results exclude ClO_4^- influence in stabilizing iodine cations.

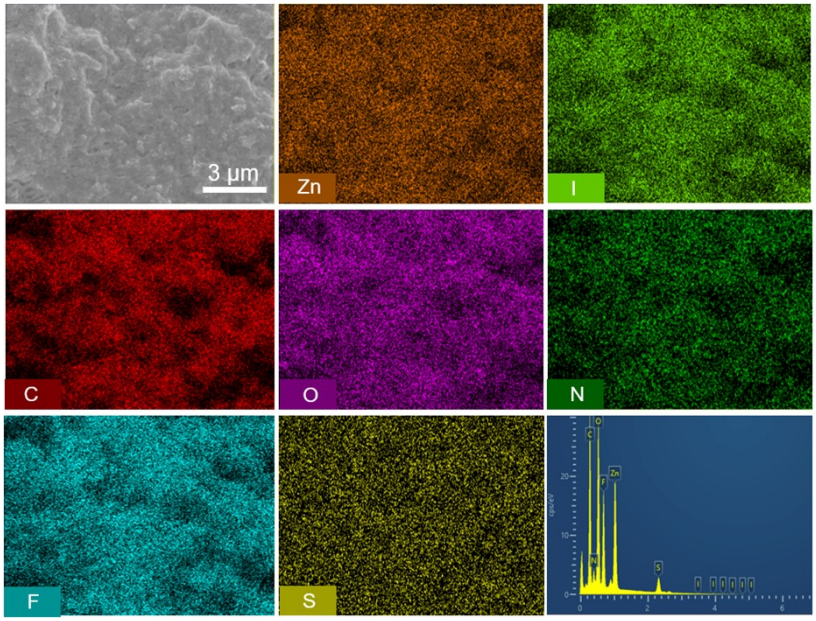

Figure S26. The EDS mapping of the I_2@C cathode after full discharge.

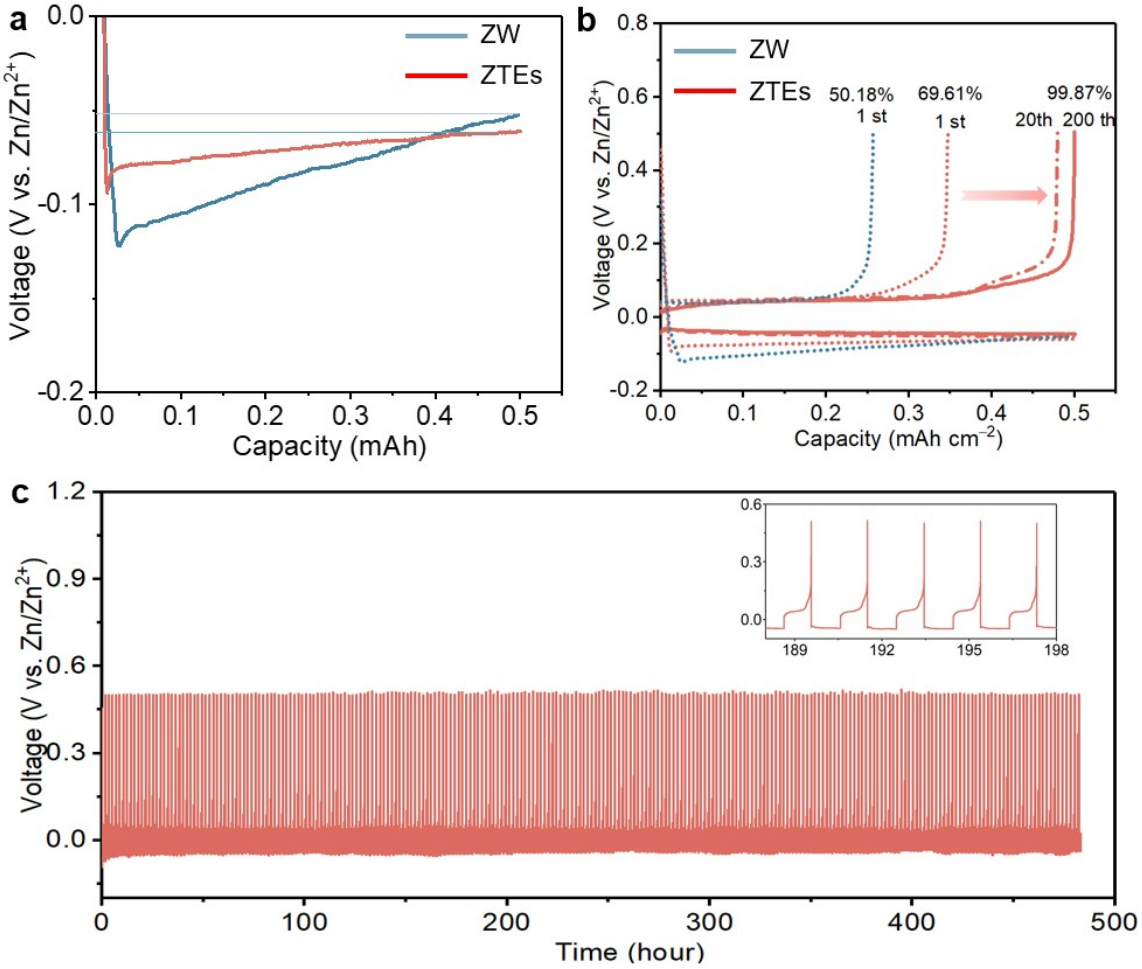

Figure S27. Zn plating/stripping performance in ZTEs. (a) Voltage profiles of galvanostatic Zn plating/stripping with the maximum oxidation potential of 0.5 V (vs. Zn/Zn^{2+}) in ZTEs and ZW at a rate of 0.5 mA cm^{-2} (0.5 mAh cm^{-2}). The working and counter electrodes are Ti and Zn, respectively. (b) Voltage profiles and corresponding Coulombic efficiency of Zn plating and stripping processes at selected cycles in different electrolytes. (c) Voltage profiles of Zn plating and stripping in ZTEs.

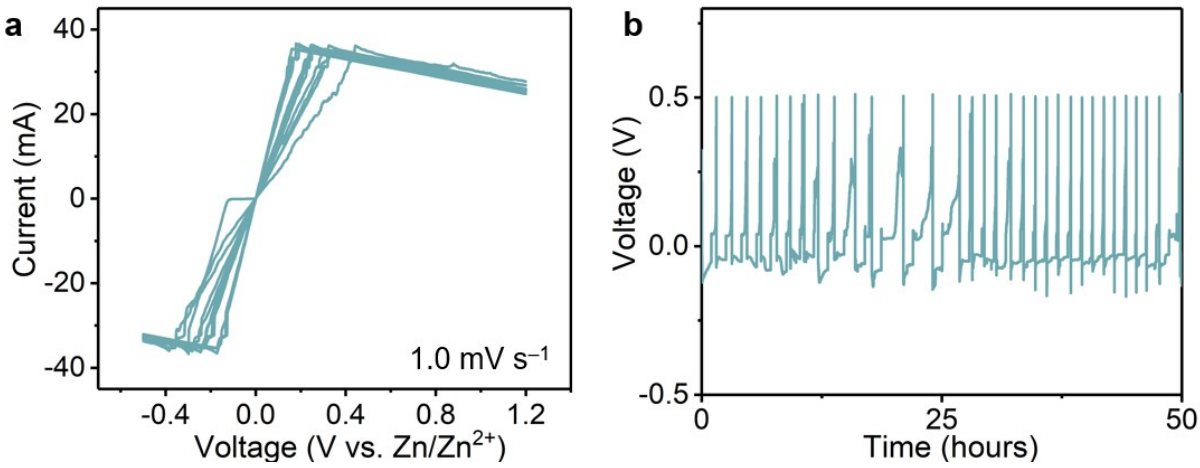

Figure S28. Zn plating/stripping in ZW. (a) Cyclic voltammetry (CV) curves of Zn plating/stripping in ZW at a scan rate of 1 mV s^{-1} with a potential range of -0.5-1.2 V. (b) Voltage-time curves of Zn plating/stripping in ZW. The working and counter electrodes are Zn and Ti, respectively.

Note: The CV curves of Zn plating/stripping in ZW demonstrate an abnormal deposition peak potential, which can be attribute to the violent side reactions on the zinc metal interface.

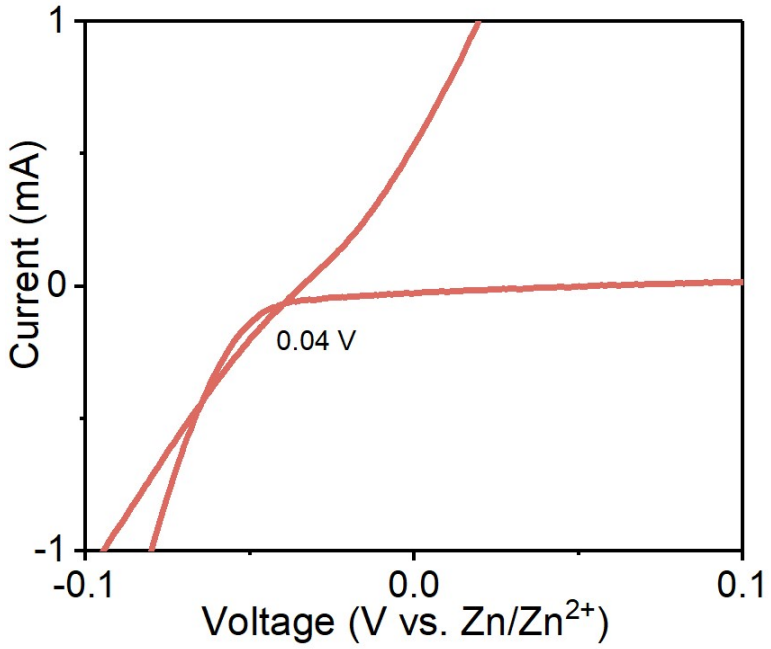

Figure S29. CV curves of ZTEs in a cell at a scan rate of 0.5 mV s^{-1}.

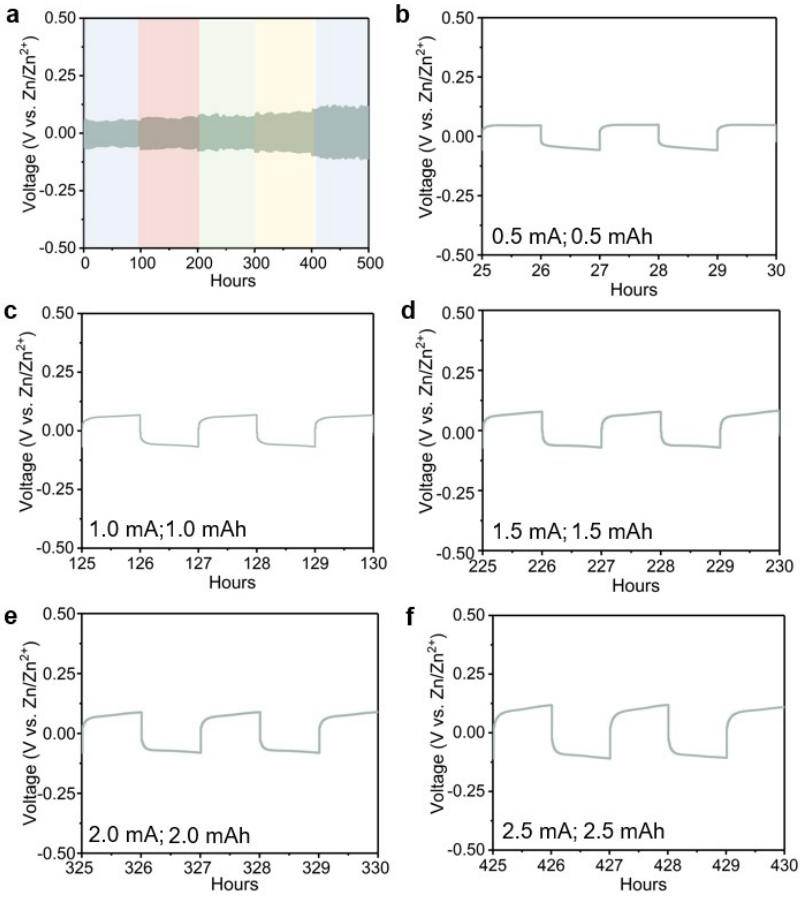

Figure S30. (a) Voltage responses of Zn/Zn cell with ZTEs at rates of 0.5-2.5 mA cm^{-2} (each half cycle lasts for 1.0 h). (b-f) The enlarged partial details voltage responses of Zn/Zn cell.

Note: The potential of ZTEs for supporting the reversible Zn electrochemistry was also investigated under galvanostatic conditions at elevated current densities from 0.5-2.5 mA cm^{-2}.

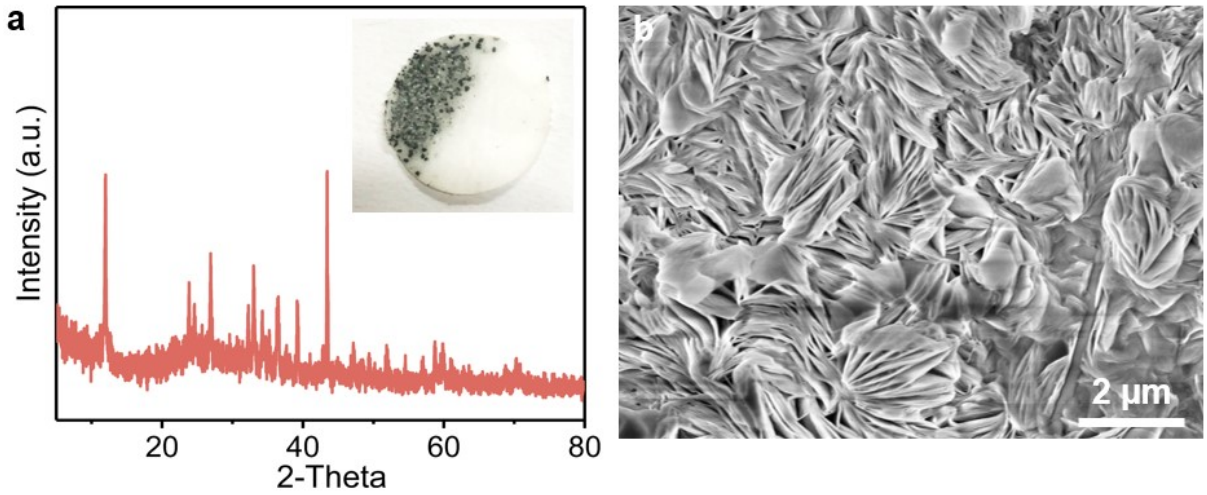

Figure S31. (a) XRD spectra and (b) SEM image of the cycled glass fiber membrane using ZW electrolyte (insert of the optical photograph).

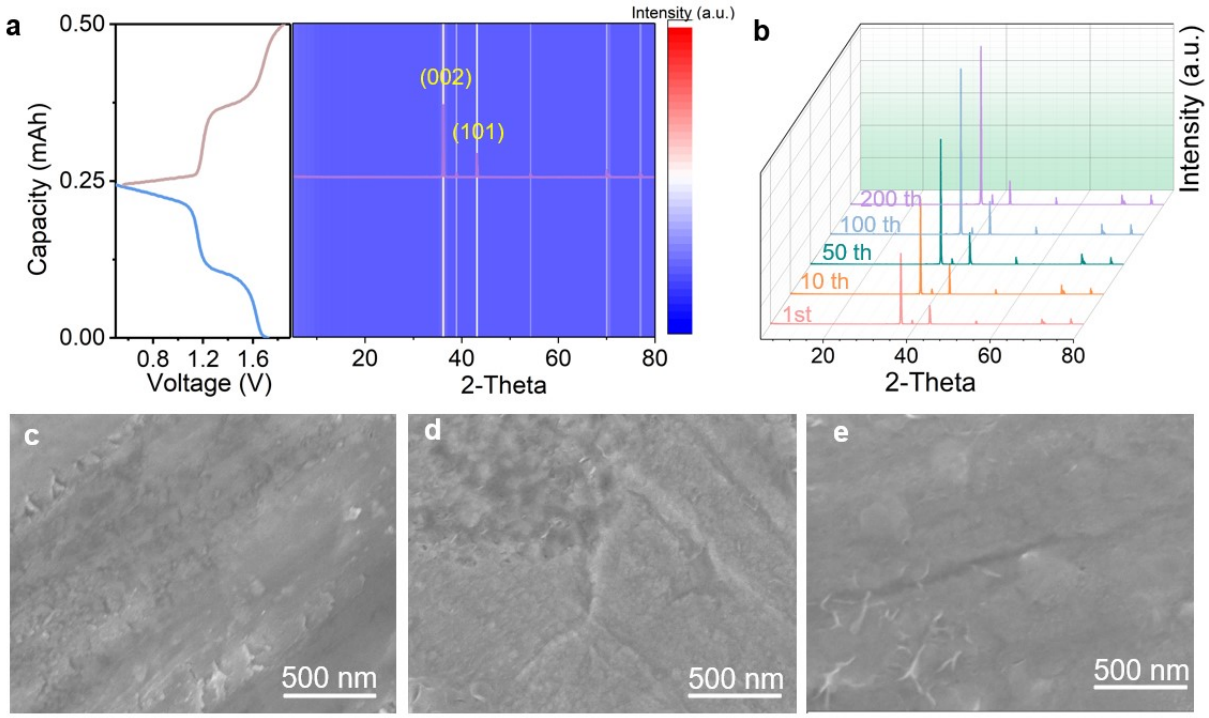

Figure S32. Characterizations of Zn anode cycled in ZTEs. (a) The *ex-situ* XRD spectra of Zn anode during charege/discharge process. (b) The XRD spectra of Zn anode after diffferent cylcles. SEM images of the Zn anode after (c) 1st (d)10th and (e) 50 cycled using ZTEs electrolyte.

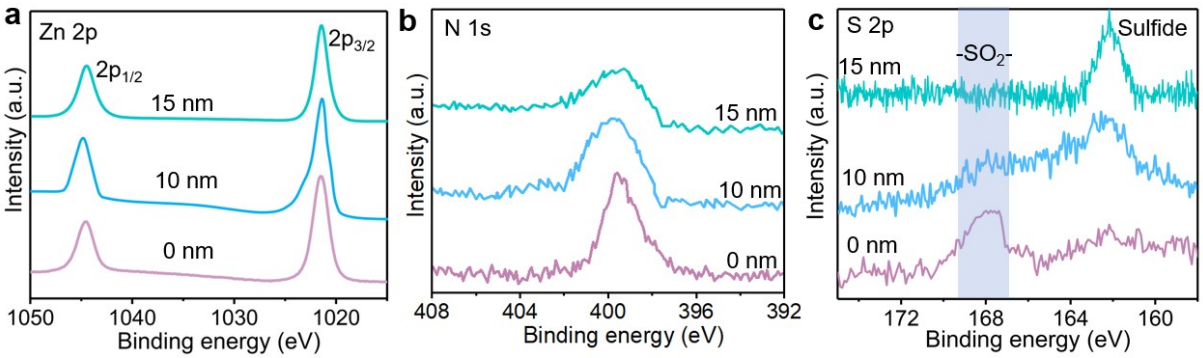

Figure S33. XPS spectral regions for Zn 2p, N 1s, and S 2p at various argon (Ar+) sputtering depths on the Zn anode after cycled in ZTEs.

Note: As the etching depth increased, the intensity of sulfide increases gradually while those of nitrides decrease, indicating that S/N-rich organic compounds are mainly distributed in the SEI layer.

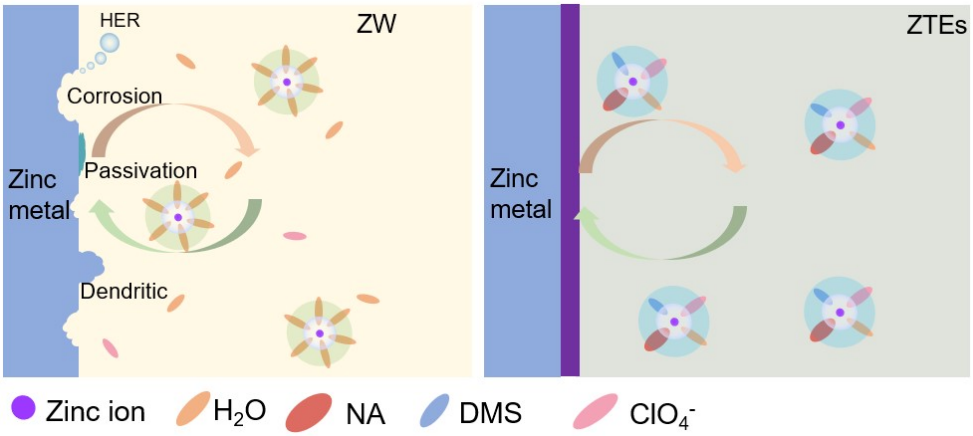

Figure S34. In the conventional electrolyte (left), intrinsic weak acidity of the electrolyte leads to uncontrolled dendrites and notorious side reactions occurring at the Zn-electrolyte interface. In the ZTEs electrolyte (right), the zincophilic effect of neutral ligands and the hydrogen bond locking with water by distinguished solvated shell structure of Zn^{2+} enables a record Zn plating/striping lifespan.

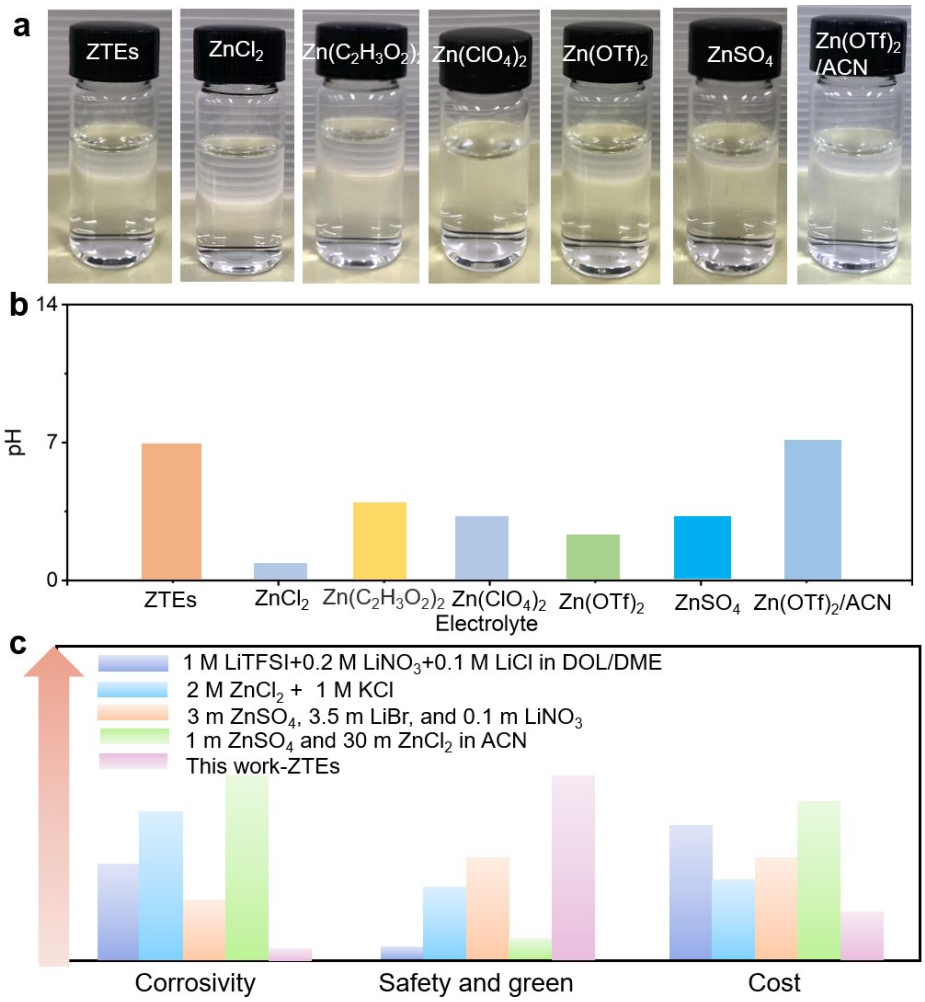

Figure S35. Comparison of commonly used Zn^{2+} electrolytes. (a) The optical photograph of commonly used Zn^{2+} electrolytes. (b) pH of the commonly used Zn^{2+} electrolytes. (c) The superiorities of the ZTEs electrolyte compared with the reported electrolytes of I_2-metal battery that realized four-electron $2I^-/I_2/2I^+$ conversion chemistry.

Note: Generally, the commonly used zinc salts for Zn-based batteries include $ZnSO_4$, $Zn(ClO_4)_2$ and $Zn(OTf)_2$, et al., there are exist plentiful protons in aqueous Zn^{2+} electrolytes due to the hydrolysis reaction of Zn salt. Therefore, the Zn anodes inevitably suffer and face hydrogen evolution and dendrite issues. Additionally, there are limited reports of chloride-containing electrolytes used to achieve the four-electron conversion of iodine, the presence of chloride ions severely corrodes battery components that greatly limiting their application. Moreover, The components of ZTEs electrolyte are green and harmless, and inexpensive. Therefore, the ZTEs electrolyte demonstrates great advantages in terms of green and cost for large-scale use.

Supplementary Tables

Table S1. Comparison of polarization voltage of this work to reported I_2-metal, Mn-Zn, and V-Zn battery systems.

Cathodes		Electrolyte	Anode type	Specific capacity	Ref.
I_2-Metal	I_2@C	ZTEs	Zn	412 mAh g^{-1} at 0.5 A g^{-1}	This work
	ACC/I_2	1M $ZnSO_4$	Zn	220 mAh g^{-1} at 0.2 A g^{-1}	(2)
	TiO_2/I_2	0.5M ZnI_2	Zn	114 mAh g^{-1} at 0.5 A g^{-1}	(3)
	ACF/I_2	1M $ZnSO_4$	Zn	174 mAh g^{-1} at 0.2 A g^{-1}	(4)
	I_2-ZIF	0.5M $ZnSO_4$	Zn	182 mAh g^{-1} at 0.2 A g^{-1}	(5)
	C/I_2	0.5M KPF_6	K	156 mAh g^{-1} at 0.05 A g^{-1}	(6)
	CMK/I_2	1M KPF_6	K	89 mAh g^{-1} at 0.5 A g^{-1}	(7)
Zn-Mn	γ-MnO_2	1M $ZnSO_4$	Zn	285 mAh g^{-1} at 0.05 A g^{-1}	(8)
	β-MnO_2	1M $ZnSO_4$	Zn	270 mAh g^{-1} at 0.1 A g^{-1}	(9)
	MnO_2	1M $ZnSO_4$ +0.2M $MnSO_4$	Zn	290 mAh g^{-1} at 0.1 A g^{-1}	(10)
	MnO_2	ZSC-gel	Zn	275 mAh g^{-1} at 0.3 A g^{-1}	(11)
	γ-MnO_2	$Zn(CF_3SO_3)_2$ +$Mn(CF_3SO_3)_2$	Zn	132 mAh g^{-1} at 0.15 A g^{-1}	(12)
	Mn_3O_4	2M $ZnSO_4$	Zn	239 mAh g^{-1} at 0.1 A g^{-1}	(13)
	δ-MnO_2	2M $ZnSO_4$ +0.2M $MnSO_4$	Zn	278 mAh g^{-1} at 0.3 A g^{-1}	(14)
Zn-V	$Zn_{0.25}V_2O_5{\cdot}nH_2O$	1M $ZnSO_4$	Zn	260 mAh g^{-1} at 0.3 A g^{-1}	(15)
	$Ca_{0.24}V_2O_5{\cdot}0.83H_2O$	1M $ZnSO_4$	Zn	180 mAh g^{-1} at 0.5 A g^{-1}	(16)
	V_2O_5	3M $Zn(CF_3SO_3)_2$	Zn	410 mAh g^{-1} at 1 A g^{-1}	(17)
	$V_2O_5{\cdot}nH_2O$	3M $Zn(CF_3SO_3)_2$	Zn	381 mAh g^{-1} at 0.06 A g^{-1}	(18)
	$H_2V_3O_8$	3M $Zn(CF_3SO_3)_2$	Zn	240 mAh g^{-1} at 1 A g^{-1}	(19)
	LiV_3O_8	1M $ZnSO_4$	Zn	188 mAh g^{-1} at 0.13 A g^{-1}	(20)
	V_2O_5/$V_3O_7{\cdot}nH_2O$	$Zn(CF_3SO_3)_2$ + LiTFSI	Zn	250 mAh g^{-1} at 0.5 A g^{-1}	(21)
Zn-Organic	PANI	3M $Zn(CF_3SO_3)_2$	Zn	174 mAh g^{-1} at 0.5 A g^{-1}	(22)
	PQ-MCT	1Zn-0.5Sc in $AcNDI_4$	Zn	120.8 mAh g^{-1} at 0.1 A g^{-1}	(23)
	PANI	$ZnCl_2$/EG	Zn	180 mAh g^{-1} at 2 A g^{-1}	(24)

	PTD-1	2 M $ZnSO_4$	Zn	145 mAh g^{-1} at 0.1 A g^{-1}	(25)
	PQ-MCT	0.5m ZnTFMS/DMF	Zn	131 mAh g^{-1} at 0.2 A g^{-1}	(26)
	PDB	$Zn(ClO4)_2$ /H_2O/SN	Zn	100 mAh g^{-1} at 50 mA g^{-1}	(27)
	HATN-PNZ	3M $Zn(CF_3SO_3)_2$	Zn	257 mAh g^{-1} at 5 A g^{-1}	(28)
	PANI	2M $ZnSO_4$ + 0.01 m SG	Zn	192 mAh g^{-1} at 1 A g^{-1}	(29)

Supplementary Calculations.

The theoretical capacity of I_2 cathode based four-electron conversion is

$$C = \frac{nF}{M} = \frac{4 \times 26800 \frac{mAh}{mol}}{2 \times 126.9 \frac{g}{mol}} = 422.4 \frac{mAh}{g}$$

The electromotive force of Zn-I_2 battery is

$$V = -\frac{\Delta Gf}{nF} = \frac{558 \frac{kJ}{mol}}{4 \times 94{,}685 \frac{C}{mol}} = 1.47\ V$$

The theoretical energy density of I_2 cathode based four-electron conversion is

$$E = C \times V = 422.4 \frac{mAh}{g} \times 1.47\ V = 621\ \text{Wh/kg}$$

The theoretical energy density of Zn-I_2 battery based four-electron conversion is

$$E = -\frac{\Delta Gf}{M} = \frac{558 \frac{kJ}{mol}}{320 \frac{g}{mol}} = 1746 \frac{kJ}{kg} = 485 \frac{Wh}{kg}$$

Supplementary References

1. Wei T, Li Q, Yang G, & Wang C Pseudo-Zn-Air and Zn-Ion Intercalation Dual Mechanisms to Realize High-Areal Capacitance and Long-Life Energy Storage in Aqueous Zn Battery. Adv. Energy Mater. **2019**, *9*, (34) 1901480.
2. Bai C*, et al.* A sustainable aqueous Zn-I_2 battery. Nano Research, **2018**, *11*: 3548-3554.
3. Man Y*, et al.* A Photo-Assisted Chargeable Aqueous Zinc-Iodine Battery. Chem Electro Chem **2019**, *6*, 5872-5875
4. Pan H*, et al.* Controlling solid-liquid conversion reactions for a highly reversible aqueous zinc-iodine battery. ACS Energy Lett. **2017**, *2*(12): 2674-2680.
5. Wang Z*, et al.* A metal-organic framework host for highly reversible dendrite-free zinc metal anodes. Joule, **2019**, *3*(5): 1289-1300.
6. Lu K*, et al.* Rechargeable potassium-ion batteries enabled by potassium-iodine conversion chemistry. Energy Storage Mater. **2019**, *16*: 1-5.
7. Qian M*, et al.* Iodine encapsulated in mesoporous carbon enabling high-efficiency capacitive potassium-Ion storage. J. colloid interface sci. **2019**, *551*: 177-183.
8. Alfaruqi MH*, et al.* Electrochemically induced structural transformation in a γ-MnO_2 cathode of a high capacity zinc-ion battery system. Chem. Mater. **2015**, *27*(10): 3609-3620.
9. Islam S*, et al.* Facile synthesis and the exploration of the zinc storage mechanism of β-MnO_2 nanorods with exposed (101) planes as a novel cathode material for high performance eco-friendly zinc-ion batteries. J. Mater. Chem. A **2017**, *44*: 23299-23309.
10. Sun W*, et al.* Zn/MnO_2 battery chemistry with H^+ and Zn^{2+} coinsertion. J. Am. Chem. Soc. **2017**, *139*(29): 9775-9778.
11. Mo F*, et al.* Zwitterionic sulfobetaine hydrogel electrolyte building separated positive/negative ion migration channels for aqueous Zn-MnO_2 batteries with superior rate capabilities. Adv. Energy Mater. **2020**, *10*(16): 2000035.
12. Zhang N*, et al.* Rechargeable aqueous zinc-manganese dioxide batteries with high energy and power densities. Nat. Commun. **2017**, *8*(1): 405.
13. Hao J*, et al.* Electrochemically induced spinel-layered phase transition of Mn_3O_4 in high performance neutral aqueous rechargeable zinc battery. Electrochimica Acta, **2018**, *259*: 170-178.

14. Wang D*, et al.* A superior δ-MnO_2 cathode and a self-healing Zn-δ-MnO2 battery. ACS Nano, **2019**, *13*(9): 10643-10652.
15. Kundu D, Adams BD, Duffort V, Vajargah SH, & Nazar LFJNE A high-capacity and long-life aqueous rechargeable zinc battery using a metal oxide intercalation cathode. Nat. Energy, **2016**, *1*(10): 1-8.
16. Yang Q*, et al.* Rechargeable aqueous Mn-metal battery enabled by inorganic–organic interfaces. Ange. Chem. Inter. Ed. **2022**, *61*(35): e202206471.
17. Zhang N*, et al.* Rechargeable aqueous Zn-V_2O_5 battery with high energy density and long cycle life. ACS Energy Lett. **2018**, *3*(6): 1366-1372.
18. Yan M*, et al.* Water-lubricated intercalation in $V_2O_5{\cdot}nH_2O$ for high-capacity and high-rate aqueous rechargeable zinc batteries. Adv. Mater. **2018**, *30*(1): 1703725.
19. He P*, et al.* High-performance aqueous zinc-ion battery based on layered $H_2V_3O_8$ nanowire cathode. Small, **2017**, *13*(47): 1702551.
20. Alfaruqi MH*, et al.* Electrochemical zinc intercalation in lithium vanadium oxide: a high-capacity zinc-ion battery cathode. Chem. Mater. **2017**, *29*(4): 1684-1694.
21. Li X*, et al.* Hydrated hybrid vanadium oxide nanowires as the superior cathode for aqueous Zn battery. Mater. Today Energy, **2019**, *14*: 100361.
22. Feng D, Jiao Y, & Wu P Proton-Reservoir Hydrogel Electrolyte for Long-Term Cycling Zn/PANI Batteries in Wide Temperature Range. Angew. Chem. Int. Ed. **2023**, *135*(1): e202215060.
23. Kim M*, et al.* Cationic Additive with a Rigid Solvation Shell for High-Performance Zinc Ion Batteries. Angew. Chem. Int. Ed. **2022**, *61*(47):e202211589.
24. Geng L*, et al.* Eutectic Electrolyte with Unique Solvation Structure for High-Performance Zinc-Ion Batteries. Angew. Chem. Int. Ed. **2022**, *134*(31): e202206717.
25. Wang N*, et al.* Molecular Tailoring of an n/p-type Phenothiazine Organic Scaffold for Zinc Batteries. Angew. Chem. Int. Ed. **2021**, *60*(38): 20826-20832.
26. Chen J*, et al.* A Desolvation-Free Sodium Dual-Ion Chemistry for High Power Density and Extremely Low Temperature. Angew. Chem. Int. Ed. **2021**, *60*(44): 23858-23862.
27. Yang W*, et al.* Hydrated Eutectic Electrolytes with Ligand-Oriented Solvation Shells for Long-Cycling Zinc-Organic Batteries. Joule **2020**, *4*(7):1557-1574.
28. Li S*, et al.* Design and Synthesis of a pi-Conjugated N-Heteroaromatic Material for

Aqueous Zinc-Organic Batteries with Ultrahigh Rate and Extremely Long Life. Adv. Mater. **2022**,:e2207115.

29. Hao J, Yuan L, Zhu Y, Jaroniec M, & Qiao SZ Triple-Function Electrolyte Regulation toward Advanced Aqueous Zn-Ion Batteries. Adv. Mater. **2022**, *34*(44):e2206963.